JOURNAL OF SPACECRAFT AND ROCKETS
Vol. 32, No. 1, January–February 1995

Attitude Dynamics Investigation of the OEDIPUS-A Tethered Rocket Payload

G. Tyc*
Bristol Aerospace Limited, Winnipeg, Manitoba R3C 2S4, Canada
and
R. P. S. Han†
University of Manitoba, Winnipeg, Manitoba R3T 2N2, Canada

The OEDIPUS-A tethered rocket payload consisted of two spinning subpayloads each with a pair of flexible radial booms and connected by a conductive tether. This first flight of a spinning tethered two-body system achieved a tether deployment of 958 m, which at that time was the longest space tether ever flown. Although the approximately 15-min mission was generally very successful, unexpected dynamic behavior was observed in one of the subpayloads. This paper reviews the attitude dynamics investigation that was undertaken following the flight in an attempt to understand what may have caused this dynamics anomaly. The formulation of a general mathematical model is described that consists of a rigid central body undergoing large rotations with three orthogonal pairs of flexible booms. Tether interaction with the central body is modeled as a forcing term, caused by the tether tension, to the free-body equations. Results of a parametric study are presented, which show that the interaction of the tether with the payload, which was assumed to be negligible prior to the flight, is the likely cause of the unexpected dynamic behavior. Two mechanisms associated with the tether interaction have been identified: one is a forcing term on the payload, which causes a precession of the payload angular momentum vector, and the other is additional energy dissipation in the payload.

Nomenclature

A–F = elements of the instantaneous moment of inertia tensor for the subpayload
a_j = radial offset of the jth boom from the spin axis
$\hat{a}_j$ = a_j/l_j
a_t = distance from the subpayload center of mass to the tether attachment point
$[C]$ = transformation matrix that relates the body-fixed frame to the inertial frame
c_{11}–c_{33} = elements of the transformation matrix (direction cosines)
d = offset of the plane of the radial booms from the subpayload center of mass
$\hat{d}_j$ = d/l_j
EI_j = beam stiffness of the jth boom
$\widehat{EI}_j$ = $EI_j/\rho_j l_j^4$
F_t = tether forcing term on the subpayload
$[I]$ = moment of inertia tensor for the subpayload including the deformed booms
l_j = length of the jth boom
m_{jk} = kth point mass along the jth boom
$\hat{m}_{jk}$ = $m_{jk}/\rho_j l_j$
N_x, N_y, N_z = components of the external torque applied to the subpayload by the tether
N_j = number of point masses on the jth boom
$Oxyz$ = body-fixed reference frame with the origin at the subpayload center of mass
$OXYZ$ = inertially fixed reference frame with the origin at the subpayload center of mass
q_{in} = generalized modal coordinate representing the ith deflection for the nth mode
T = rotational kinetic energy of the complete subpayload
u_i = deformations of the flexible booms
V = potential energy associated with the booms
$\{\Gamma\}$ = angular momentum vector due to boom deformation
δ_{nm} = Kronecker delta
ξ = nondimensionalized distance along a boom (equals 0 at the root and 1 at the tip)
ξ_{jk} = location of the kth point mass along the jth boom
ρ_j = linear mass density of the jth boom
ϕ_{jn} = admissible function for the jth boom and the nth mode
Ω_{jn} = natural frequency of vibration associated with the nth mode of the jth boom
$\{\omega\}$ = absolute angular velocity vector of the body-fixed frame

Subscripts

i = boom deformation
j = boom element
n, m = mode numbers
x, y, z = axes of the body-fixed frame

Introduction

ON January 30, 1989, the Canadian OEDIPUS-A tethered payload was successfully launched on a three-stage Black Brant 10 sounding rocket from the Andoya launch site in northern Norway. The project was sponsored and managed by the Space Science Division of the Canadian Space Agency (CSA) and involved scientists from Canada and the United States. The primary objectives of the OEDIPUS (Observations of Electric-field Distributions in the Ionospheric Plasma—a Unique Strategy) experiment were to: make passive observations of the auroral ionosphere, in particular, directly measure the weak dc electric field parallel to the Earth's magnetic field by using the tethered payload as a large double probe; measure the response of the large double probe in the ionospheric plasma; and seek new insights into plane-wave and sheath-wave propagation in plasmas by using a radio transmitter on the forward payload and a synchronized receiver on the aft payload. The flight successfully achieved the scientific objectives listed above and, at that time,

Received April 1, 1993; revision received May 16, 1994; accepted for publication May 18, 1994.

*Mechanical Systems Engineer, Space Systems Group, Rockets and Space Division, 660 Berry Street, P.O. Box 874. Member AIAA.

†Associate Professor, Department of Mechanical and Industrial Engineering. Senior Member AIAA.

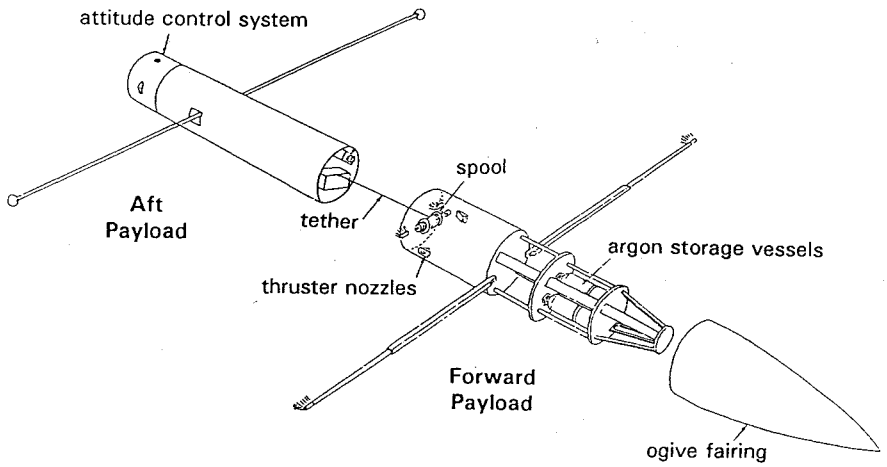

Fig. 1 OEDIPUS-A payload configuration.

established a new record for the maximum length of a space tether (958 m).[1]

The OEDIPUS-A payload comprised two subpayloads (i.e., end bodies of the two-body tethered configuration), which are referred to as the forward and aft payloads, as shown in Fig. 1. Each cylindrical subpayload had radial flexible booms and was spun about its minimum-moment-of-inertia axis (i.e., the axis of symmetry). The tether connecting the subpayloads was very thin and under very low tension; hence it was assumed that it would have negligible effects on the subpayload dynamics over the course of the approximately 15-min flight. Therefore, the preflight attitude dynamics analysis assumed that each subpayload was a freely spinning body. Since the subpayloads were minor-axis spinners, the well-known major-axis rule clearly states that they were unstable, as the flexible booms provided a source of energy dissipation.[2,3] Consequently payload coning was inevitable, as each subpayload will naturally approach a flat spin orientation about its major axis (a dynamically stable configuration) at a rate that is related to the energy dissipation in each subpayload. Flying unstable payloads such as OEDIPUS-A is not unusual for sounding rocket flights, however, since because of the short flight duration, it is possible to contain the coning angle to within acceptable limits by minimizing the energy dissipation rate. For OEDIPUS-A, the energy dissipation rate was predicted prior to the flight by modeling the boom dynamics resulting from the payload coning and using an experimentally measured damping factor for the booms. This analysis was conducted by the NASA Sounding Rocket Division at Wallops Island, which routinely conducts this type of analysis for all its sounding rocket flights that include flexible booms. The analysis predicted that the coning angle of the aft payload should remain well within 10 deg (note that the coning angle in this paper means the half-angle of the cone swept out by the spin axis during one precession cycle). The forward payload was not investigated, as it had shorter and much stiffer booms than the aft payload and hence its coning would progress at a much slower rate than that of the aft payload.

Flight dynamics data from the OEDIPUS-A mission indicated that the subpayloads did not behave as expected. The aft payload was observed to have reached a coning angle of nearly 40 deg towards the end of the flight. Additionally, its dynamic behavior during the payload separation phase was not characteristic of a freely spinning body as assumed in the preflight analysis. The forward payload, on the other hand, behaved more or less as expected, with a coning angle of approximately 7 deg throughout the flight.

This paper describes the postflight payload dynamics analysis that was undertaken in an attempt to understand what might have caused this unexpected dynamic behavior.[4,5] The preflight predictions of the payload coning angles, developed by NASA, were based on the assumption that the tether would not significantly influence the payload dynamics over the course of the flight. Additionally, the mathematical model used by NASA included a number of simplifying assumptions (e.g., small angles, axisymmetric payload, pitch-axis moment of inertia much greater than the roll-axis moment of inertia). The postflight investigation therefore focused on the development of a more comprehensive mathematical model of the OEDIPUS subpayloads that allowed large three-degree-of-freedom angular rotations of the payload, included flexible cantilevered booms with mounting offsets and point masses, and also included a simplified tether interaction model. This general flexible spacecraft configuration has received much attention in the technical literature dating back to the mid 1960s.[6–12] Modi provides a good review of the dynamical analyses conducted for this class of systems.[13] The formulation used in this present investigation is similar to that employed by Vigneron[7] in the study of the Alouette and ISIS satellites, but is extended to allow for axial booms, point masses along each boom, and offsets of the boom attachments from the system center of mass, as these elements are important for the OEDIPUS configuration. Additionally, the tether interaction is incorporated as a forcing term to the system equations. Numerical simulation code that incorporated the equations of motion was developed, and a parametric study was undertaken to investigate the possible range of parameter values that are needed to reproduce the flight data.

The OEDIPUS-A payload and mission sequence are described. The formulation of the equations of motion is then summarized, and computer simulation results are presented and compared with the flight data. The parametric investigation is then described, and it is shown that the observed motions in the aft payload are likely caused by the interaction of the tether wire.

Description of the OEDIPUS-A Payload and Mission Sequence

The OEDIPUS-A payload configuration is depicted in Fig. 1. After jettisoning the payload fairing and experiment doors, the fore and aft payloads had masses of 84 and 131 kg, respectively, and each had its own complement of scientific instruments, control, power, and telemetry systems. The forward and aft payload properties are summarized in Table 1 in the flight configuration. The radial booms on the fore and aft payloads were used as dipoles for the plasma plane-wave propagation experiments. An attitude control system (ACS) module, located at the aft end of the aft payload, was used to despin the complete payload to 0.71 cps after the third-stage motor burnout and align the spin axis to within 1 deg of the Earth's magnetic field prior to payload separation. Approximately 1200 m of Teflon-coated, stranded tin-copper tether wire, slightly less than 1 mm in diameter, was wound on a spool-type reel located on the forward payload, and the free end attached to an instrument on the aft payload. To separate the two subpayloads, pressurized argon gas was fed through thrusters in the forward payload to impart a predetermined relative velocity between the payloads. A magnetic hysteresis brake was attached to the spool assembly to apply a small constant torque to the spool as the tether was deployed to smoothly

decelerate the relative motion of the payloads. Because of the sensitivity of the measurements being made, active attitude control of the subpayloads was not permitted during experimentation, as any gas expulsion or magnetic field generation could contaminate the experiments. Therefore, passive spin stabilization was used following payload separation. A more complete description of the OEDIPUS-A payload is given by Eliuk et al.[14]

The OEDIPUS-A payload flight sequence is illustrated in Fig. 2. Shortly after motor burnout, the fairing was jettisoned along with a number of experiment doors, and the two sets of radial booms were deployed. The forward payload booms should have been nearly 2 m long; however, they did not open fully, and it was estimated that they were actually less than a meter long, as indicated in Table 1.

Table 1 OEDIPUS-A forward and aft payload properties

Parameter	Forward payload	Aft payload
Payload mass, kg	84	131
Spin rate, cps	0.71	0.71
A_0, kg-m^2	24.27	36.59
B_0, kg-m^2	24.39	39.24
C_0, kg-m^2	1.84	5.88
Boom length, m	0.88	2.57
Boom base radial offset, m	0.146	0.18
Effective boom mass rate, kg/m	0.367	0.134
Tip mass, kg	0.015	0.054
Effective boom EI, N-m^2	3750[a]	57.4
Hysteretic energy loss per stress cycle	Not measured	10%
Boom material	Fiberglass	Be-Cu

[a]Approximated.

At $T + 121$ s, the ACS maneuver was initiated, which aligned the payload to within 1 deg of the local geomagnetic field line. At this point, pyrotechnic bolt cutters released the manacle ring that connected the fore and aft payloads, and compression springs initiated the payload separation. The pressurized argon thrusters were then fired for approximately 15 s to create the required relative velocity between the two subpayloads. The thrusters were shut off once a predetermined angular velocity was observed in the tether spool. After this point, the magnetic hysteresis brake on the spool was slowly decelerating the relative motion between the subpayloads. At $T + 448$ s, apogee was reached and payload separation was completed with a separation distance of 958 m. This configuration is maintained for the remainder of the flight. Because of the gravity-gradient torque on the two-body system, the entire configuration experienced a slight rotation throughout the flight. At approximately $T + 800$ s the payload re-entered the atmosphere and was not recovered.

Magnetometer data from both the fore and aft payloads were collected during the flight and were used to compute the angular deviation of each payload from the magnetic field vector, which is presented in Fig. 3. Since the magnetic field vector remains nearly fixed over the trajectory, the plots given in Fig. 3 provide a reasonable estimate of the payload coning. The flight data indicate that the forward payload experienced a tipoff at separation that caused a coning angle of approximately 7 deg which varied only slightly (i.e., several degrees) throughout the flight. The aft payload, on the other hand, exhibited significantly different behavior. The data indicate that the aft payload also experienced a tipoff at separation and the resulting coning angle was approximately 3.5 deg. However, unlike that of the forward payload, the coning angle began to increase at an unexpectedly high rate, so

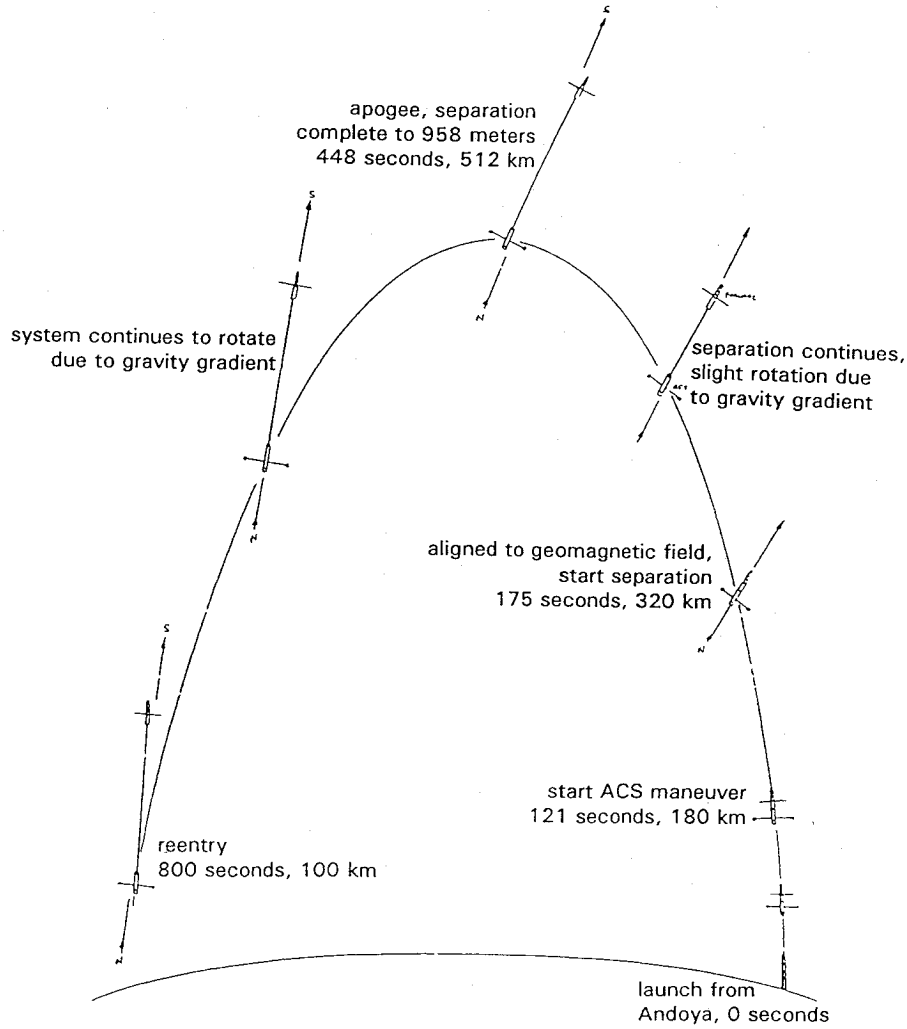

Fig. 2 OEDIPUS-A flight sequence.

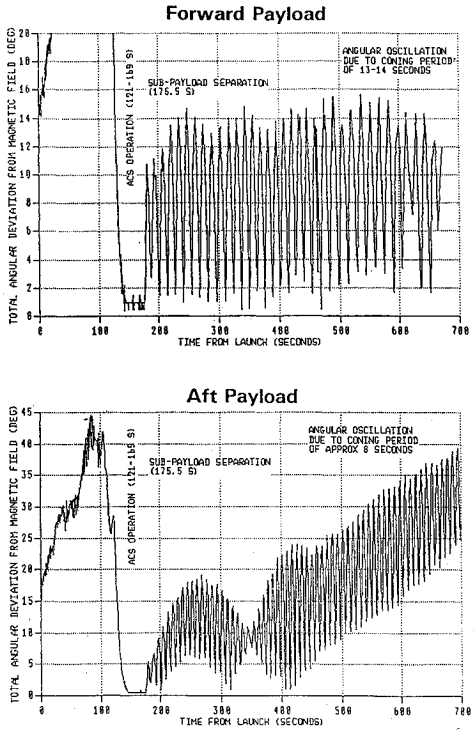

Fig. 3 OEDIPUS-A flight data.

that it approached 40 deg towards the end of the flight, which far exceeded the predicted value. Additionally, the data indicate that the aft payload experienced some other motions not characteristic of a torque-free body during the first 225 s following payload separation, which coincides with the separation phase of the flight.

Payload Dynamics Model

To investigate the possible causes of the unexpected dynamic behavior of the aft payload during the flight, a generalized mathematical model was developed, which comprises a central rigid body with three orthogonal pairs of flexible booms, as shown in Fig. 4. An arbitrary number of point masses along each flexible boom are also included. The reference axes $(Oxyz)$ are fixed to the central body with the origin located on the mass center of the entire system, and the x axis aligned so that it is always parallel to the base of boom 1. The interaction of the tether is included as the forcing term F_t, which creates a torque about the payload's mass center. The motivation for developing a generalized model was to allow modeling both the OEDIPUS-A configuration and a planned future OEDIPUS mission, referred to as OEDIPUS-B, which included the full complement of booms as well as tip and midspan sensors.[4]

The formulation of the equations of motion is based on the following assumptions: 1) the deformations of the booms are small; 2) the booms have symmetric cross sections; 3) the booms have a constant linear mass density with an arbitrary number of point masses; 4) axial deformation of the booms is negligible; and 5) the mass center of the system remains fixed during deformation of the booms. The equations of motion are derived using variational principles with each boom characterized as a linearly elastic continuum. A hybrid coordinate formulation, similar to that used by Likins,[15] is employed, where modal coordinates are used to describe the deformation of the booms while discrete coordinates are used to describe the three rotational degrees of freedom of the central rigid body.

The deformation of the booms is represented by the following:

$$u_i = \sum_n l_j q_{in}(t)\phi_{jn}(\xi) \tag{1}$$

In this analysis, the cantilever modes of vibration of an Euler-Bernoulli beam are used as the set of comparison functions [which is a subset of the set of admissible functions $\phi_{jn}(\xi)$]. Using Eq. (1), and retaining only first- and second-order terms, the kinetic and potential energy expressions for the system can be written as follows:

$$\begin{aligned} T = {} & \tfrac{1}{2}\{\omega\}^T[I]\{\omega\} + \{\omega\}^T\{\Gamma\} \\ & + \frac{1}{2}\sum_n \left[\rho_1 l_1^3 M_{1n}\left(\dot{q}_{1n}^2 + \dot{q}_{3n}^2 + \dot{q}_{5n}^2 + \dot{q}_{7n}^2\right)\right. \\ & + \rho_2 l_2^3 M_{2n}\left(\dot{q}_{2n}^2 + \dot{q}_{4n}^2 + \dot{q}_{6n}^2 + \dot{q}_{8n}^2\right) \\ & \left. + \rho_3 l_3^3 M_{3n}\left(\dot{q}_{9n}^2 + \dot{q}_{10n}^2\right) + \rho_4 l_4^3 M_{4n}\left(\dot{q}_{11n}^2 + \dot{q}_{12n}^2\right)\right] \end{aligned} \tag{2}$$

$$\begin{aligned} V = {} & \frac{1}{2}\sum_n \left[\rho_1 l_1^3 \widehat{EI}_1 R_{1n}\left(q_{1n}^2 + q_{3n}^2 + q_{5n}^2 + q_{7n}^2\right)\right. \\ & + \rho_2 l_2^3 \widehat{EI}_2 R_{2n}\left(q_{2n}^2 + q_{4n}^2 + q_{6n}^2 + q_{8n}^2\right) \\ & \left. + \rho_3 l_3^3 \widehat{EI}_3 R_{3n}\left(q_{9n}^2 + q_{10n}^2\right) + \rho_4 l_4^3 \hat{E} I_4 R_{4n}\left(q_{11n}^2 + q_{12n}^2\right)\right] \end{aligned} \tag{3}$$

where M_{jn}, R_{jn} are flexural coefficients involving the comparison functions $\phi_{jn}(\xi)$. The elements of the instantaneous inertia tensor $[I]$ are defined as follows:

$$[I] = \begin{bmatrix} A & -F & -E \\ & B & -D \\ \text{sym} & & C \end{bmatrix} \tag{4}$$

The expressions for the elements of the instantaneous inertia tensor are given below (boom foreshortening has been taken into account):

$$\begin{aligned} A = {} & A_0 + \sum_n \left[\rho_1 l_1^3 M_{1n}\left(q_{1n}^2 + q_{3n}^2 + q_{5n}^2 + q_{7n}^2\right)\right. \\ & \left. + \rho_2 l_2^3 M_{2n}\left(q_{6n}^2 + q_{8n}^2\right) + \rho_3 l_3^3 M_{3n} q_{9n}^2 + \rho_4 l_4^3 M_{4n} q_{11n}^2\right] \\ & - \sum_n \sum_m \left[\rho_2 l_2^3 (\varepsilon_{2nm} + \hat{a}_2 \epsilon_{2nm})(q_{2n}q_{2m} + q_{4n}q_{4m}\right. \\ & \left. + q_{6n}q_{6m} + q_{8n}q_{8m}) + \rho_3 l_3^3 (\varepsilon_{3nm} + \hat{a}_3 \epsilon_{3nm})(q_{9n}q_{9m}\right. \\ & \left. + q_{10n}q_{10m}) + \rho_4 l_4^3 (\varepsilon_{4nm} + \hat{a}_4 \epsilon_{4nm})(q_{11n}q_{11m} + q_{12n}q_{12m})\right] \end{aligned} \tag{5a}$$

$$\begin{aligned} B = {} & B_0 + \sum_n \left[\rho_1 l_1^3 M_{1n}\left(q_{5n}^2 + q_{7n}^2\right) + \rho_2 l_2^3 M_{2n}\right. \\ & \times \left(q_{2n}^2 + q_{4n}^2 + q_{6n}^2 + q_{8n}^2\right) + \rho_3 l_3^3 M_{3n} q_{10n}^2 \\ & \left. + \rho_4 l_4^3 M_{4n} q_{12n}^2\right] - \sum_n \sum_m \left[\rho_1 l_1^3 (\varepsilon_{1nm} + \hat{a}_1 \epsilon_{1nm})\right. \\ & \times (q_{1n}q_{1m} + q_{3n}q_{3m} + q_{5n}q_{5m} + q_{7n}q_{7m}) \\ & + \rho_3 l_3^3 (\varepsilon_{3nm} + \hat{a}_3 \epsilon_{3nm})(q_{9n}q_{9m} + q_{10n}q_{10m}) \\ & \left. + \rho_4 l_4^3 (\varepsilon_{4nm} + \hat{a}_4 \epsilon_{4nm})(q_{11n}q_{11m} + q_{12n}q_{12m})\right] \end{aligned} \tag{5b}$$

$$\begin{aligned} C = {} & C_0 + \sum_n \left[\rho_1 l_1^3 M_{1n}\left(q_{1n}^2 + q_{3n}^2\right) + \rho_2 l_2^3 M_{2n}\left(q_{2n}^2 + q_{4n}^2\right)\right. \\ & \left. + \rho_3 l_3^3 M_{3n}\left(q_{9n}^2 + q_{10n}^2\right) + \rho_4 l_4^3 M_{4n}\left(q_{11n}^2 + q_{12n}^2\right)\right] \\ & - \sum_n \sum_m \left[\rho_1 l_1^3 (\varepsilon_{1nm} + \hat{a}_1 \epsilon_{1nm})(q_{1n}q_{1m} + q_{3n}q_{3m}\right. \\ & \left. + q_{5n}q_{5m} + q_{7n}q_{7m}) + \rho_2 l_2^3 (\varepsilon_{2nm} + \hat{a}_2 \epsilon_{2nm})\right. \\ & \left. \times (q_{2n}q_{2m} + q_{4n}q_{4m} + q_{6n}q_{6m} + q_{8n}q_{8m})\right] \end{aligned} \tag{5c}$$

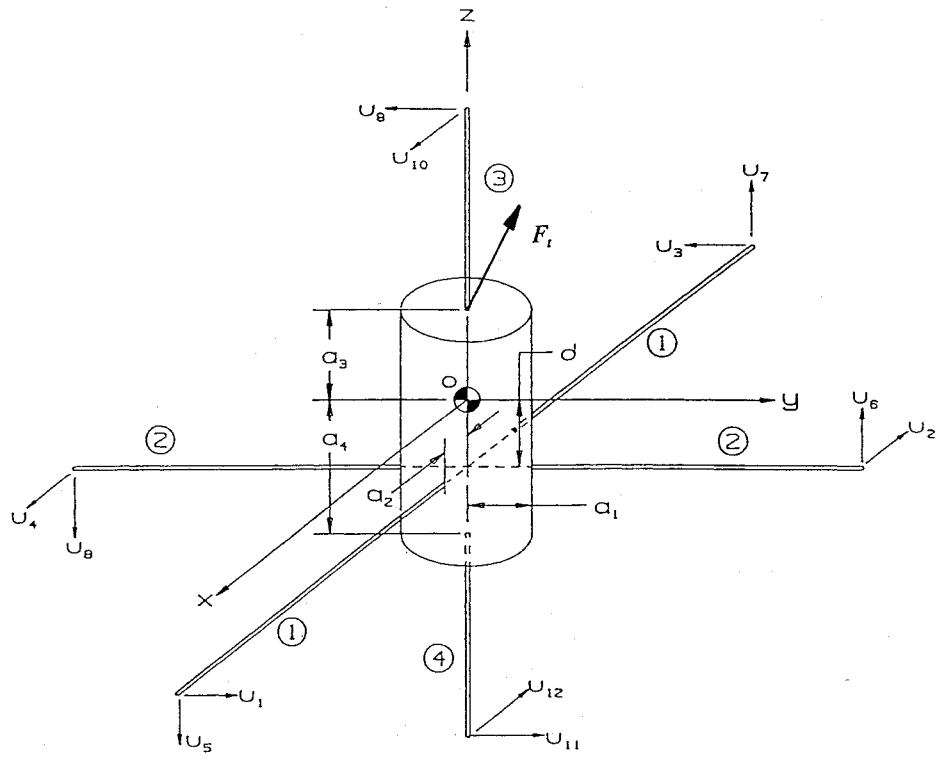

Fig. 4 Generalized mathematical model of the OEDIPUS payload configuration.

$$D = D_0 + \sum_n \Big[-\rho_1 l_1^3 M_{1n}(q_{1n}q_{5n} + q_{3n}q_{7n}) + \rho_2 l_2^3 (P_{2n} + \hat{a}_2 K_{2n})(q_{6n} + q_{8n}) - \rho_3 l_3^3 \big(P_{3n} + \hat{a}_3 K_{3n}\big) q_{9n} - \rho_4 l_4^3 (P_{4n} + \hat{a}_4 K_{4n}) q_{11n} \Big] \tag{5d}$$

$$E = E_0 + \sum_n \Big[-\rho_1 l_1^3 (P_{1n} + \hat{a}_1 K_{1n})(q_{5n} + q_{7n}) - \rho_2 l_2^3 M_{2n}(q_{2n}q_{6n} + q_{4n}q_{8n}) + \rho_3 l_3^3 (P_{3n} + \hat{a}_3 K_{3n}) q_{10n} - \rho_4 l_4^4 (P_{4n} + \hat{a}_4 K_{4n}) q_{12n} \Big] \tag{5e}$$

$$F = F_0 + \sum_n \Big[\rho_1 l_1^3 (P_{1n} + \hat{a}_1 K_{1n})(q_{1n} + q_{3n}) - \rho_2 l_2^3 (P_{2n} + \hat{a}_2 K_{2n})(q_{2n} + q_{4n}) - \rho_3 l_3^3 M_{3n} q_{9n} q_{10n} - \rho_4 l_4^4 M_{4n} q_{11n} q_{12n} \Big] \tag{5f}$$

where $A_0, B_0, \ldots, F_0$ are the elements of the inertia tensor for the undeformed configuration. The elements of $\{\Gamma\}$ are defined as follows:

$$\Gamma_x = \sum_n \Big[\rho_1 l_1^3 \{ M_{1n}(\dot{q}_{1n}q_{5n} + \dot{q}_{3n}q_{7n} - \dot{q}_{5n}q_{1n} - \dot{q}_{7n}q_{3n}) + \hat{d}_1 K_{1n}(\dot{q}_{1n} - \dot{q}_{3n}) \} + \rho_2 l_2^3 (P_{2n} + \hat{a}_2 K_{2n})(\dot{q}_{6n} + \dot{q}_{8n}) + \rho_3 l_3^3 (P_{3n} + \hat{a}_3 K_{3n}) \dot{q}_{9n} + \rho_4 l_4^3 (P_{4n} + \hat{a}_4 K_{4n}) \dot{q}_{11n} \Big] \tag{6a}$$

$$\Gamma_y = \sum_n \Big[\rho_2 l_2^3 \{ M_{2n}(q_{2n}\dot{q}_{6n} + q_{4n}\dot{q}_{8n} - q_{6n}\dot{q}_{2n} - q_{8n}\dot{q}_{4n}) + \hat{d}_2 K_{2n}(\dot{q}_{2n} - \dot{q}_{4n}) \} + \rho_1 l_1^3 (P_{1n} + \hat{a}_1 K_{1n})(\dot{q}_{5n} + \dot{q}_{7n}) + \rho_3 l_3^3 (P_{3n} + \hat{a}_3 K_{3n}) \dot{q}_{10n} + \rho_4 l_4^3 (P_{4n} + \hat{a}_4 K_{4n}) \dot{q}_{12n} \Big] \tag{6b}$$

$$\Gamma_z = \sum_n \Big[\rho_1 l_1^3 (P_{1n} + \hat{a}_1 K_{1n})(\dot{q}_{1n} + \dot{q}_{3n}) + \rho_2 l_2^3 (P_{2n} + \hat{a}_2 K_{2n}) \times (\dot{q}_{2n} + \dot{q}_{4n}) + \rho_3 l_3^3 M_{3n}(q_{9n}\dot{q}_{10n} - q_{10n}\dot{q}_{9n}) + \rho_4 l_4^3 M_{4n}(q_{11n}\dot{q}_{12n} - q_{12n}\dot{q}_{11n}) \Big] \tag{6c}$$

The flexural coefficients used in the above expressions are defined as follows:

$$M_{jn} = \int_0^1 [\phi_{jn}(\xi)]^2 d\xi + \sum_{k=1}^{N_j} \hat{m}_{jk} [\phi_{jn}(\xi_{jk})]^2,$$

$$P_{jn} = \int_0^1 \xi \phi_{jn}(\xi) d\xi + \sum_{k=1}^{N_j} \hat{m}_{jk} \xi_{jk} \phi_{jn}(\xi_{jk})$$

$$K_{jn} = \int_0^1 \phi_{jn}(\xi)\, d\xi + \sum_{k=1}^{N_j} \hat{m}_{jk} \phi_{jn}(\xi_{jk}),$$

$$R_{jn} = \int_0^1 \big[\phi''_{jn}(\xi)\big]^2 d\xi$$

$$\varepsilon_{jnm} = \int_0^1 \frac{1-\xi^2}{2} \phi'_{jn}(\xi)\phi'_{jm}(\xi)\, d\xi + \sum_{k=1}^{N_j} \hat{m}_{jk}\xi_{jk} \int_0^{\xi_{jk}} \phi'_{jn}(\xi)\phi'_{jm}(\xi)\, d\xi$$

$$\epsilon_{jnm} = \int_0^1 (1-\xi)\phi'_{jn}(\xi)\phi'_{jm}(\xi)\, d\xi + \sum_{k=1}^{N_j} \hat{m}_{jk} \int_0^{\xi_{jk}} \phi'_{jn}(\xi)\phi'_{jm}(\xi)\, d\xi$$

Lagrange's equations are used to develop the equations of motion. The generalized coordinates of this system are the elements of the angular velocity vector $\{\omega_x, \omega_y, \omega_z\}$ and $\{q_{in}\}$ with $n = 1, 2, \ldots$ and $i = 1, \ldots, 12$. The quantities $\omega_x, \omega_y, \omega_z$ are not displacements, but nonintegrable velocities, and are thus termed quasicoordinates. For these Lagrange's equations take the form[16]

$$\frac{\mathrm{d}}{\mathrm{d}t}\left(\frac{\partial L}{\partial \omega_x}\right) - \omega_z \frac{\partial L}{\partial \omega_y} + \omega_y \frac{\partial L}{\partial \omega_z} = N_x \tag{7a}$$

$$\frac{\mathrm{d}}{\mathrm{d}t}\left(\frac{\partial L}{\partial \omega_y}\right) - \omega_x \frac{\partial L}{\partial \omega_z} + \omega_z \frac{\partial L}{\partial \omega_x} = N_y \tag{7b}$$

$$\frac{\mathrm{d}}{\mathrm{d}t}\left(\frac{\partial L}{\partial \omega_z}\right) - \omega_y \frac{\partial L}{\partial \omega_x} + \omega_x \frac{\partial L}{\partial \omega_y} = N_z \tag{7c}$$

and Lagrange's equations for the set $\{q_{in}\}$ are

$$\frac{\mathrm{d}}{\mathrm{d}t}\left(\frac{\partial L}{\partial \dot{q}_{in}}\right) - \frac{\partial L}{\partial q_{in}} = Q_i \tag{8}$$

where the Lagrangian is defined as $L = T - V$, and Q_i represents the viscous damping forces in each of the booms. To determine the attitude of the payload, the elements of the transformation matrix (direction cosines) are used as attitude variables. Initially it is assumed that the $OXYZ$ axes are coincident with the $Oxyz$ axes the instant prior to payload separation. The differential equation that relates the attitude to the angular velocity is

$$[\dot{C}] = -[\omega^{\times}][C] \tag{9}$$

where $[\omega^{\times}]$ is the skew-symmetric matrix made up of the angular velocity components.

The equations of motion are derived by substituting the Eqs. (1–6) into the above Eqs. (7–9) and carrying out the necessary algebraic manipulations. The full nonlinear equations are given below:

$$\begin{aligned} &A\dot{\omega}_x - F\dot{\omega}_y - E\dot{\omega}_z + \dot{A}\omega_x - \dot{F}\omega_y - \dot{E}\omega_z \\ &\quad + (C - B)\omega_y\omega_z + D\left(\omega_z^2 - \omega_y^2\right) + F\omega_x\omega_z \\ &\quad - E\omega_x\omega_y + \dot{\Gamma}_x + \omega_y\Gamma_z - \omega_z\Gamma_y = N_x \end{aligned} \tag{10a}$$

$$\begin{aligned} &B\dot{\omega}_y - D\dot{\omega}_z - F\dot{\omega}_x + \dot{B}\omega_y - \dot{D}\omega_z - \dot{F}\omega_x \\ &\quad + (A - C)\omega_x\omega_z + E\left(\omega_x^2 - \omega_z^2\right) + D\omega_x\omega_y \\ &\quad - F\omega_y\omega_z + \dot{\Gamma}_y + \omega_z\Gamma_x - \omega_x\Gamma_z = N_y \end{aligned} \tag{10b}$$

$$\begin{aligned} &C\dot{\omega}_z - D\dot{\omega}_y - E\dot{\omega}_x + \dot{C}\omega_z - \dot{D}\omega_y - \dot{E}\omega_x \\ &\quad + (B - A)\omega_x\omega_y + F\left(\omega_y^2 - \omega_x^2\right) + E\omega_y\omega_z \\ &\quad - D\omega_x\omega_z + \dot{\Gamma}_z + \omega_x\Gamma_y - \omega_y\Gamma_x = N_z \end{aligned} \tag{10c}$$

$$\begin{aligned} &\ddot{q}_{1n} + \eta_1 \frac{\mathcal{M}_{1n}}{M_{1n}}\Omega_{1n}\dot{q}_{1n} + \left[\widehat{EI}_1 \frac{R_{1n}}{M_{1n}}\delta_{nm} - \delta_{nm}\omega_x^2 \right. \\ &\quad \left. + \frac{\varepsilon_{1nm} + \hat{a}_1\epsilon_{1nm}}{M_{1n}}\omega_y^2 + \left(\frac{\varepsilon_{1nm} + \hat{a}_1\epsilon_{1nm}}{M_{1n}} - \delta_{nm}\right)\omega_z^2\right] q_{1m} \\ &\quad + 2\omega_x\dot{q}_{5n} + (\dot{\omega}_x - \omega_y\omega_z)q_{5n} + \frac{P_{1n} + \hat{a}_1 K_{1n}}{M_{1n}} \\ &\quad \times (\dot{\omega}_z + \omega_x\omega_y) + \hat{d}_1 \frac{K_{1n}}{M_{1n}}\dot{\omega}_x = 0 \end{aligned} \tag{10d}$$

$$\begin{aligned} &\ddot{q}_{2n} + \eta_2 \frac{\mathcal{M}_{2n}}{M_{2n}}\Omega_{2n}\dot{q}_{2n} + \left[\widehat{EI}_2 \frac{R_{2n}}{M_{2n}}\delta_{nm} + \frac{\varepsilon_{2nm} + \hat{a}_2\epsilon_{2nm}}{M_{2n}}\omega_x^2 \right. \\ &\quad \left. - \delta_{nm}\omega_y^2 + \left(\frac{\varepsilon_{2nm} + \hat{a}_2\epsilon_{2nm}}{M_{2n}} - \delta_{nm}\right)\omega_z^2\right] q_{2m} - 2\omega_y\dot{q}_{6n} \\ &\quad - (\dot{\omega}_y + \omega_x\omega_z)q_{6n} + \frac{P_{2n} + \hat{a}_2 K_{2n}}{M_{2n}}(\dot{\omega}_z - \omega_x\omega_y) \\ &\quad + \hat{d}_2 \frac{K_{2n}}{M_{2n}}\dot{\omega}_y = 0 \end{aligned} \tag{10e}$$

$$\begin{aligned} &\ddot{q}_{3n} + \eta_1 \frac{\mathcal{M}_{1n}}{M_{1n}}\Omega_{1n}\dot{q}_{3n} + \left[\widehat{EI}_1 \frac{R_{1n}}{M_{1n}}\delta_{nm} - \delta_{nm}\omega_x^2 \right. \\ &\quad \left. + \frac{\varepsilon_{1nm} + \hat{a}_1\epsilon_{1nm}}{M_{1n}}\omega_y^2 + \left(\frac{\varepsilon_{1nm} + \hat{a}_1\epsilon_{1nm}}{M_{1n}} - \delta_{nm}\right)\omega_z^2\right] q_{3m} \\ &\quad + 2\omega_x\dot{q}_{7n} + (\dot{\omega}_x - \omega_y\omega_z)q_{7n} + \frac{P_{1n} + \hat{a}_1 K_{1n}}{M_{1n}} \\ &\quad \times (\dot{\omega}_z + \omega_x\omega_y) - \hat{d}_1 \frac{K_{1n}}{M_{1n}}\dot{\omega}_x = 0 \end{aligned} \tag{10f}$$

$$\begin{aligned} &\ddot{q}_{4n} + \eta_2 \frac{\mathcal{M}_{2n}}{M_{2n}}\Omega_{2n}\dot{q}_{4n} + \left[\widehat{EI}_2 \frac{R_{2n}}{M_{2n}}\delta_{nm} + \frac{\varepsilon_{2nm} + \hat{a}_2\epsilon_{2nm}}{M_{2n}}\omega_x^2 \right. \\ &\quad \left. - \delta_{nm}\omega_y^2 + \left(\frac{\varepsilon_{2nm} + \hat{a}_2\epsilon_{2nm}}{M_{2n}} - \delta_{nm}\right)\omega_z^2\right] q_{4m} \\ &\quad - 2\omega_y\dot{q}_{8n} - (\dot{\omega}_y + \omega_x\omega_z)q_{8n} \\ &\quad + \frac{P_{2n} + \hat{a}_2 K_{2n}}{M_{2n}}(\dot{\omega}_z - \omega_x\omega_y) - \hat{d}_2 \frac{K_{2n}}{M_{2n}}\dot{\omega}_y = 0 \end{aligned} \tag{10g}$$

$$\begin{aligned} &\ddot{q}_{5n} + \eta_1 \frac{\mathcal{M}_{1n}}{M_{1n}}\Omega_{1n}\dot{q}_{5n} + \left[\widehat{EI}_1 \frac{R_{1n}}{M_{1n}}\delta_{nm} - \delta_{nm}\omega_x^2 \right. \\ &\quad \left. + \left(\frac{\varepsilon_{1nm} + \hat{a}_1\epsilon_{1nm}}{M_{1n}} - \delta_{nm}\right)\omega_y^2 + \frac{\varepsilon_{1nm} + \hat{a}_1\epsilon_{1nm}}{M_{1n}}\omega_z^2\right] q_{5m} \\ &\quad - 2\omega_x\dot{q}_{1n} - (\dot{\omega}_x + \omega_y\omega_z)q_{1n} \\ &\quad + \frac{P_{1n} + \hat{a}_1 K_{1n}}{M_{1n}}(\dot{\omega}_y - \omega_x\omega_z) = 0 \end{aligned} \tag{10h}$$

$$\begin{aligned} &\ddot{q}_{6n} + \eta_2 \frac{\mathcal{M}_{2n}}{M_{2n}}\Omega_{2n}\dot{q}_{6n} + \left[\widehat{EI}_2 \frac{R_{2n}}{M_{2n}}\delta_{nm} \right. \\ &\quad \left. + \left(\frac{\varepsilon_{2nm} + \hat{a}_2\epsilon_{2nm}}{M_{2n}} - \delta_{nm}\right)\omega_x^2 - \delta_{nm}\omega_y^2 \right. \\ &\quad \left. + \frac{\varepsilon_{2nm} + \hat{a}_2\epsilon_{2nm}}{M_{2n}}\omega_z^2\right] q_{6m} + 2\omega_y\dot{q}_{2n} + (\dot{\omega}_y - \omega_x\omega_z)q_{2n} \\ &\quad + \frac{P_{2n} + \hat{a}_2 K_{2n}}{M_{2n}}(\dot{\omega}_x + \omega_y\omega_z) = 0 \end{aligned} \tag{10i}$$

$$\begin{aligned} &\ddot{q}_{7n} + \eta_1 \frac{\mathcal{M}_{1n}}{M_{1n}}\Omega_{1n}\dot{q}_{7n} + \left[\widehat{EI}_1 \frac{R_{1n}}{M_{1n}}\delta_{nm} - \delta_{nm}\omega_x^2 \right. \\ &\quad \left. + \left(\frac{\varepsilon_{1nm} + \hat{a}_1\epsilon_{1nm}}{M_{1n}} - \delta_{nm}\right)\omega_y^2 \right. \\ &\quad \left. + \frac{\varepsilon_{1nm} + \hat{a}_1\epsilon_{1nm}}{M_{1n}}\omega_z^2\right] q_{7m} - 2\omega_x\dot{q}_{3n} - (\dot{\omega}_x + \omega_y\omega_z)q_{3n} \\ &\quad + \frac{P_{1n} + \hat{a}_1 K_{1n}}{M_{1n}}(\dot{\omega}_y - \omega_x\omega_z) = 0 \end{aligned} \tag{10j}$$

$$\ddot{q}_{8n} + \eta_2 \frac{\mathcal{M}_{2n}}{M_{2n}} \Omega_{2n} \dot{q}_{8n} + \left[\widehat{EI}_2 \frac{R_{2n}}{M_{2n}} \delta_{nm} + \left(\frac{\varepsilon_{2nm} + \hat{a}_2 \epsilon_{2nm}}{M_{2n}} - \delta_{nm} \right) \omega_x^2 - \delta_{nm} \omega_y^2 + \frac{\varepsilon_{2nm} + \hat{a}_2 \epsilon_{2nm}}{M_{2n}} \omega_z^2 \right] q_{8m} + 2\omega_y \dot{q}_{4n} + (\dot{\omega}_y - \omega_x \omega_z) q_{4n} + \frac{P_{2n} + \hat{a}_2 K_{2n}}{M_{2n}} (\dot{\omega}_x + \omega_y \omega_z) = 0 \tag{10k}$$

$$\ddot{q}_{9n} + \eta_3 \frac{\mathcal{M}_{3n}}{M_{3n}} \Omega_{3n} \dot{q}_{9n} + \left[\widehat{EI}_3 \frac{R_{3n}}{M_{3n}} \delta_{nm} + \left(\frac{\varepsilon_{3nm} + \hat{a}_3 \epsilon_{3nm}}{M_{3n}} - \delta_{nm} \right) \omega_x^2 + \frac{\varepsilon_{3nm} + \hat{a}_3 \epsilon_{3nm}}{M_{3n}} \omega_y^2 - \delta_{nm} \omega_z^2 \right] q_{9m} - 2\omega_z \dot{q}_{10n} - (\dot{\omega}_z + \omega_x \omega_y) q_{10n} + \frac{P_{3n} + \hat{a}_3 K_{3n}}{M_{3n}} (\dot{\omega}_x - \omega_y \omega_z) = 0 \tag{10l}$$

$$\ddot{q}_{10n} + \eta_3 \frac{\mathcal{M}_{3n}}{M_{3n}} \Omega_{3n} \dot{q}_{10n} + \left[\widehat{EI}_3 \frac{R_{3n}}{M_{3n}} \delta_{nm} + \frac{\varepsilon_{3nm} + \hat{a}_3 \epsilon_{3nm}}{M_{3nm}} \omega_x^2 + \left(\frac{\varepsilon_{3nm} + \hat{a}_3 \epsilon_{3nm}}{M_{3n}} - \delta_{nm} \right) \omega_y^2 - \delta_{nm} \omega_z^2 \right] q_{10m} + 2\omega_z \dot{q}_{9n} + (\dot{\omega}_z - \omega_x \omega_y) q_{9n} + \frac{P_{3n} + \hat{a}_3 K_{3n}}{M_{3n}} (\dot{\omega}_y + \omega_x \omega_z) = 0 \tag{10m}$$

$$\ddot{q}_{11n} + \eta_4 \frac{\mathcal{M}_{4n}}{M_{4n}} \Omega_{4n} \dot{q}_{11n} + \left[\widehat{EI}_4 \frac{R_{4n}}{M_{4n}} \delta_{nm} + \left(\frac{\varepsilon_{4nm} + \hat{a}_4 \epsilon_{4nm}}{M_{4n}} - \delta_{nm} \right) \omega_x^2 + \frac{\varepsilon_{4nm} + \hat{a}_4 \epsilon_{4nm}}{M_{4n}} \omega_y^2 - \delta_{nm} \omega_z^2 \right] q_{11m} - 2\omega_z \dot{q}_{12n} - (\dot{\omega}_z + \omega_x \omega_y) q_{12n} + \frac{P_{4n} + \hat{a}_4 K_{4n}}{M_{4n}} (\dot{\omega}_x - \omega_y \omega_z) = 0 \tag{10n}$$

$$\ddot{q}_{12n} + \eta_4 \frac{\mathcal{M}_{4n}}{M_{4n}} \Omega_{4n} \dot{q}_{12n} + \left[\widehat{EI}_4 \frac{R_{4n}}{M_{4n}} \delta_{nm} + \frac{\varepsilon_{4nm} + \hat{a}_4 \epsilon_{4nm}}{M_{4n}} \omega_x^2 + \left(\frac{\varepsilon_{4nm} + \hat{a}_4 \epsilon_{4nm}}{M_{4n}} - \delta_{nm} \right) \omega_y^2 - \delta_{nm} \omega_z^2 \right] q_{12m} + 2\omega_z \dot{q}_{11n} + (\dot{\omega}_z - \omega_x \omega_y) q_{11n} + \frac{P_{4n} + \hat{a}_4 K_{4n}}{M_{4n}} (\dot{\omega}_y + \omega_x \omega_z) = 0 \tag{10o}$$

$$\begin{aligned} \dot{c}_{12} &= c_{22}\omega_z - c_{32}\omega_y \\ \dot{c}_{22} &= c_{32}\omega_x - c_{12}\omega_z \\ \dot{c}_{32} &= c_{12}\omega_y - c_{22}\omega_x \\ \dot{c}_{13} &= c_{23}\omega_z - c_{33}\omega_y \\ \dot{c}_{23} &= c_{33}\omega_x - c_{13}\omega_z \\ \dot{c}_{33} &= c_{13}\omega_y - c_{23}\omega_x \end{aligned} \tag{10p}$$

where summation is implied on the index m, and the coefficient $\mathcal{M}_{jn}$ is defined as follows:

$$\mathcal{M}_{jn} = \int_0^1 \phi_n^2(\xi)\, \mathrm{d}\xi$$

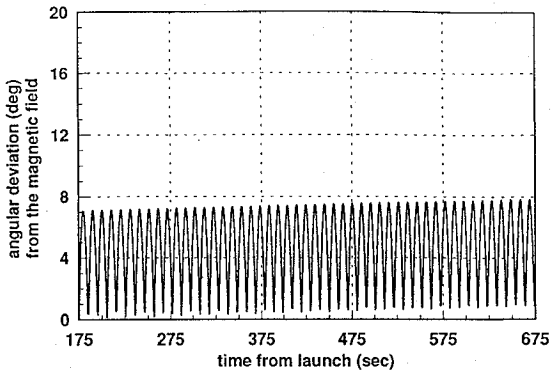

Fig. 5 Simulation results for the aft payload with no tether interaction.

The remaining elements of the transformation matrix can be found from the following relationships:

$$\begin{aligned} c_{11} &= c_{22}c_{33} - c_{23}c_{32} \\ c_{21} &= c_{32}c_{13} - c_{33}c_{12} \\ c_{31} &= c_{12}c_{23} - c_{13}c_{22} \end{aligned} \tag{10q}$$

Equations (10) form the complete equations of motion for the model depicted in Fig. 4. The direction cosines can be used to determine the physical attitude variables such as the Euler angles by using the appropriate relations.

The equations of motion have been coded in FORTRAN 77 and solved numerically using the IMSL routine DIVPAG, which is based on Gear's method,[17] a well-known and widely used numerical integration technique suitable for stiff systems of equations. Using system parameters that are appropriate to the OEDIPUS-A aft payload, setting N_x, N_y, N_z to zero (i.e., assuming no tether interaction), and using the appropriate initial conditions (i.e., tipoff at separation), the computer simulation results were found to agree extremely well with the analysis conducted by NASA prior to the flight. The simulation results for the OEDIPUS-A aft payload are given in Fig. 5; it is assumed that the Earth's magnetic field vector is inertially fixed. This latter assumption is justified, as the magnetic field vector orientation moves only a few degrees over the entire flight trajectory. On comparing these results with the flight data given in Fig. 3, it is clear that they are not in agreement. This indicates that the boom vibrations alone are likely not the cause of the anomalous dynamic behavior observed in the aft payload.

Parametric Study

To investigate if the tether interaction could be the reason for the unexpected dynamic behavior observed in OEDIPUS-A, a simple tether interaction model was formulated and included in the simulation code.[18] The tether tension provides a force on the aft payload as shown in Fig. 6, where the orientation of this force vector is defined relative to a nonrotating frame $Ox'y'z'$. The motion of this force vector is defined by prescribed evolution histories for the orientation angles θ and ϕ. The expressions for the torque imparted to the payload due to the tether force are

$$\begin{aligned} N_x &= -a_t F_t [c_{21} \sin\theta \cos\phi + c_{22} \sin\theta \sin\phi + c_{23} \cos\theta] \\ N_y &= a_t F_t [c_{11} \sin\theta \cos\phi + c_{12} \sin\theta \sin\phi + c_{13} \cos\theta] \\ N_z &= 0 \end{aligned} \tag{11}$$

The external torque expressions (11) are substituted into Eqs. (10a–10c) to complete the equations of motion. Note that the torque expressions involve the direction cosines, which are used as the attitude variables in this mathematical model. A parametric study was then conducted that investigated the dynamic behavior of the end body with various combinations of force magnitudes and force-vector motions. To limit the range of parameter values to investigate, postflight analyses described in the following paragraph were used to provide some practical bounds on the parameter values.

Based on extensive attitude determination studies of the OEDIPUS-A aft payload that were conducted following the flight, the first using predominantly magnetometer data[19] and the second

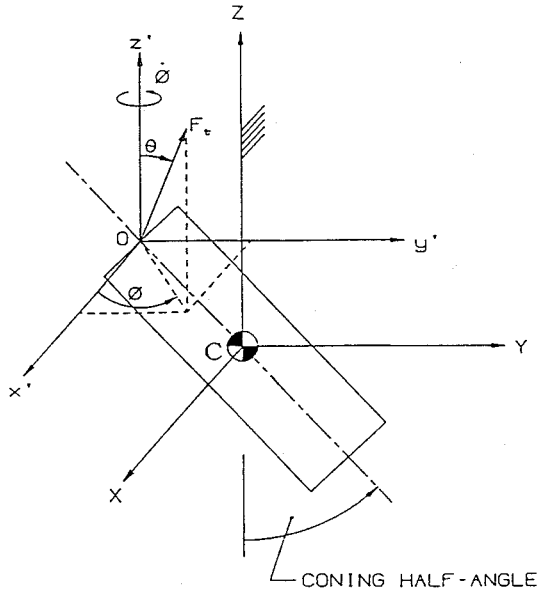

Fig. 6 Tether force model for OEDIPUS-A.

using exclusively star data from a CCD video camera mounted on the aft payload,[20] it was found that the payload angular momentum vector had a precessional type of motion up to approximately $T + 450$ s, which coincides with the completion of the payload separation phase. This motion, along with a steadily increasing coning angle, accounts for the type of payload dynamic behavior observed during this period. At $T + 450$ s, the momentum vector suddenly becomes nearly fixed in inertial space while the coning angle continues to increase. This implies that the tether tension, which is primarily created by the payload separation forces (i.e., motion of the subpayloads and a constant brake torque applied to the tether spool) and applies the predominant external torque to the subpayloads, suddenly drops off to very near zero once full separation is achieved. This is consistent with mathematical modeling results that imply that the payloads should experience a slight recoil at the end of the separation and thus the tether tension should become near zero almost instantaneously. Since the gravity gradient forces tend to pull the payloads apart, tension would again be established in the tether, but only to very low levels (approximately 0.13 N). From inspection of the flight data on the aft payload given in Fig. 3, it appears that there is also another possible scenario for the period following $T + 450$ s, where the coning angle is more or less constant and the momentum vector is continually shifting. However, in view of the attitude determination studies that were conducted, this scenario was found to be impossible. The analysis of the CCD video camera data[20] also determined the orientation of the nominal tether in inertial space (i.e., the line connecting the fore and aft payloads), as the forward payload had a beacon light that could be seen in the video data. This analysis showed that, due primarily to a tipoff of the forward payload at separation, the nominal tether line was approximately 7–8 deg from the magnetic field for the flight time following payload separation. The accuracy of this estimate is expected to be within ±2 deg. Finally, by analyzing the data from a shaft encoder that was mounted to the tether deployment spool, the nominal tether tension during the flight was determined. It was found that following an initial tension spike caused by the initiation of payload separation, the tether tension slowly increased from just below 1 N to nearly 2 N.

Given the flight data described above, the following gives the ranges of parameter values for the tether interaction model that were investigated: $F_t \leq 2$ N during subpayload separation; $F_t = 0$ N following the completion of subpayload separation at $T + 450$ s; θ is constant and between 5 and 10 deg with 7 deg as nominal; and the following simple model was assumed for the angle ϕ:

$$\phi = \phi_0 + \dot{\phi} t$$

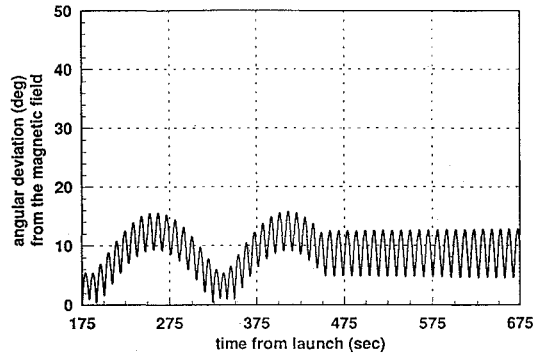

Fig. 7 Simulation results for the aft payload with tether interaction.

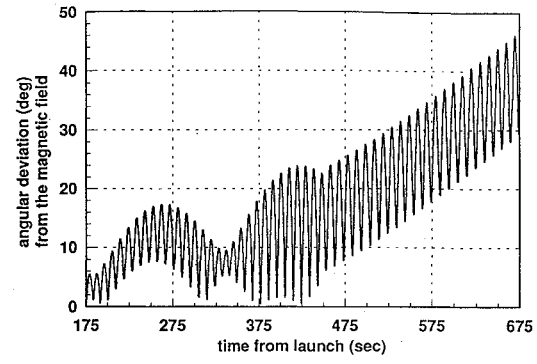

Fig. 8 Simulation results for the aft payload with tether interaction and increased boom damping.

where t is the time after payload separation, ϕ_0 is the initial value for ϕ, and $\dot{\phi}$ is a constant angular rate. The parameter values for F_t, θ, ϕ_0, and $\dot{\phi}$ were varied, and the simulation results were compared with the flight data. Reasonable agreement was found with $F_t = 1$ N during subpayload separation and $F_t = 0$ N after separation, $\theta = 7$ deg, $\phi_0 = 126$ deg, and $\dot{\phi} = 0.65$ deg/s. The simulation results are shown in Fig. 7.

The difference between the flight data in Fig. 3 for the aft payload and the simulation data given in Fig. 7 appears to be primarily in the rate at which the coning angle is increasing. This more rapid coning-angle increase evident in the flight data implies that more energy is being removed from the payload than could be accounted for by the boom vibration. It is believed that this may be either because energy is transferred from the aft payload to the tether and/or because the tether is exciting the flexible booms and thus causing more energy to be dissipated in the booms than that caused purely by the payload dynamics. To test this hypothesis, the damping factor in the booms was increased well beyond the experimentally derived value to allow for more energy to be dissipated. This was done because the booms are the only energy-dissipating mechanism that is included in the mathematical model. Good agreement was found with the flight data for a boom damping factor of 160%, as shown in Fig. 8. Note that this damping factor implies that 160% of the boom vibrational energy is dissipated during each oscillation cycle. Clearly, this is not a realistic value for the booms, as the experimentally determined value is 10%. This result strongly suggests that the added energy dissipation is related to the tether interaction, as there is no other damping mechanism on the payload or environmental disturbance (e.g., aerodynamic torque) that can account for this level of damping in the payload.

To assess if the tether interaction model that was used for the aft payload is valid, the payload mathematical model with the tether interaction included was applied to the smaller forward payload. In this case, the booms were only partially deployed and were very stiff (see Table 1), so that the boom vibration is negligible and hence no energy dissipation is expected from the booms. The result of the simulation is shown in Fig. 9 for the period following payload separation, assuming a deployed boom configuration as given in Table 1 and no damping (i.e., no internal energy dissipation in the

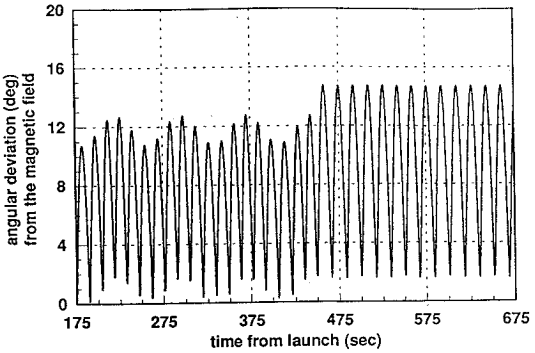

Fig. 9 Simulation results for the forward payload with tether interaction.

payload). Note that there is reasonably good agreement between the simulation and the flight data for the forward payload, given in Fig. 3, for the period up to $T+450$ s. Both plots show that there is a cyclic oscillation with a period of nearly 100 s, and the average angular deviation from the magnetic field stays more or less constant. There are some differences, of course, particularly following $T + 450$ s; however, that is to be expected, as the payload properties are only estimated (since the actual deployed boom configuration is not known) and the tether interaction model is greatly simplified. Figure 9 shows that the simulation results have the same general trends as the flight data, and hence supports the tether interaction model discussed above. Finally, it is worth noting that, unlike the aft payload, it was not neccessary to introduce increased energy dissipation by the forward payload in order to provide a reasonable fit to the flight data.

Conclusions

In this paper, the OEDIPUS-A sounding rocket mission was described that flew a spin-stabilized tethered payload that achieved a 958-m tether deployment. This first flight of a spinning tethered two-body system experienced some unexpected dynamic behavior in one of the subpayloads (i.e., end bodies). The postflight analysis, conducted to investigate the cause of this dynamical anomaly, was described. A generalized mathematical model of a spacecraft was presented that included a rigid central core with three orthogonal pairs of flexible booms and a simplified tether interaction model. The model allows for large rotational motions of the central body and small-amplitude vibration of the flexible booms. The analysis described in this paper suggests that interaction of the tether with the aft subpayload was the likely cause of its unexpected dynamic behavior. It appears that there are two mechanisms associated with the tether that have influenced the aft subpayload dynamics:

1) The tether tension exerts an external torque on the subpayload, which causes its momentum vector to precess in inertial space.

2) The tether interaction causes the subpayload to lose rotational energy. This loss in energy may be due to energy transfer between the subpayload and the tether and/or due to increased energy dissipation in the flexible booms, which are excited by the tether.

Although reasonably good agreement was found between simulation results and the flight data for both the forward and aft payloads, it remains unclear at this time why the tether did not cause an energy loss in the forward payload as it did in the aft payload. It is speculated that this difference in dynamic behavior may possibly be attributed to the different mass properties of the forward payload, to the tether spool (which is located on the forward payload), and/or to tether interaction with the significantly more flexible booms on the aft payload. Clearly, a more detailed analysis is needed to fully understand the complex dynamics of this spinning two-body tethered system with flexible appendages. The analysis presented here is more qualitative in nature, intended primarily to identify the cause of the unexpected dynamic behavior.

References

[1]James, H. G., and Whalen, B. A., "OEDIPUS-A: Space Research with a New Tether," *EOS, Transactions of the American Geophysical Union*, Vol. 84, No. 12, 1991, pp. 499–506.

[2]Hughes, P. C., "Effect of Internal Energy Dissipation on the Directional Stability of Spinning Bodies," *Spacecraft Attitude Dynamics*, 1st ed., Wiley, New York, 1986, pp. 139–155.

[3]Rimrott, F. P. J., "Attitude Drift Rate and Attitude Stability," *Introductory Attitude Dynamics*, 1st ed., Springer-Verlag, New York, 1989, pp. 205–209.

[4]Tyc, G., "Boom Definition Study for Project OEDIPUS-B," Bristol Aerospace Ltd., ER 89819/A, Winnipeg, MB, Canada, Jan. 1989.

[5]Tyc, G., Han, R. P. S., and Berry, T. G., "An Investigation of the Unexpected Attitude Dynamics Experienced by the OEDIPUS-A Tethered Sounding Rocket Payload," *Proceedings of the Thirteenth Canadian Congress of Applied Mechanics*, Univ. of Manitoba, Winnipeg, MB, Canada, 1991, Vol. 2, pp. 746–747.

[6]Etkin, B., "Spin Decay of a Flexible Satellite by Structural Dissipation of Energy," Inst. for Aerospace Studies, Univ. of Toronto, Report 105, Toronto, ON, Canada, Mar. 1965.

[7]Vigneron, F. R., "Stability of a Freely Spinning Satellite of Crossed-Dipole Configuration," *C.A.S.I. Transactions*, Vol. 3, No. 1, 1970, pp. 8–19.

[8]Vigneron, F. R., and Boresi, A. P., "Effect of the Earth's Gravitational Forces on the Flexible Crossed-Dipole Satellite Configuration: Part 1—Configurational Stability and Despin," *C.A.S.I. Transactions*, Vol. 3, No. 2, 1970, pp. 115–126.

[9]Vigneron, F. R., "Effect of the Earth's Gravitational Forces on the Flexible Crossed-Dipole Satellite Configuration: Part 2—Attitude Stability," *C.A.S.I. Transactions*, Vol. 3, No. 2, 1970, pp. 127–134.

[10]Kulla, P., "Dynamics of Spinning Bodies Containing Elastic Rods," *J. Spacecraft*, Vol. 9, No. 4, 1972, pp. 246–253.

[11]Meirovitch, L., and Calico, R. A., "Stability of Motion of Force-Free Spinning Satellites with Flexible Appendages," *Journal of Spacecraft and Rockets*, Vol. 9, No. 4, 1972, pp. 237–245.

[12]Rimrott, F., and Vigneron, F. R., "Mechanics of the Flexible Dipole Antenna of WISP," AIAA Paper 83-0433, Jan. 1983.

[13]Modi, V. J., "Attitude Dynamics of Satellites with Flexible Appendages—a Brief Review," *Journal of Spacecraft and Rockets*, Vol. 11, No. 11, 1974, pp. 743–751.

[14]Eliuk, W., Sobchuk, C., Rob, R., Walkty, I., Walsh, K., James, G., Whalen, B. A., and Rumbold, G., "Development of the OEDIPUS-A Sounding Rocket Payload," Fifth Conference on Astronautics, Canadian Aeronautics and Space Inst., Ottawa, ON, Canada, Nov. 1988.

[15]Likins, P. W., "Finite Element Appendage Equations for Hybrid Coordinate Dynamic Analysis," *International Journal of Solids and Structures*, Vol. 8, No. 5, 1972, pp. 709–731.

[16]Meirovitch, L., "Hybrid State Equations of Motion for Flexible Bodies in Terms of Quasi-Coordinates," *Journal of Guidance, Control, and Dynamics*, Vol. 14, No. 5, 1991, pp. 1008–1013.

[17]Gear, C. W., *Numerical Integral-Value Problems in Ordinary Differential Equations*, Prentice-Hall, Englewood Cliffs, NJ, 1971, pp. 155–167.

[18]Tyc, G., Han, R. P. S., Vigneron, F. R., Modi, V. J., Misra, A. K., and Berry, T. G., "Tether Dynamics Investigations for the Canadian OEDIPUS Sounding Rocket Program," *Proceedings of the AIAA/AAS Astrodynamics Conference* (Hilton Head Island, SC), AIAA, Washington, DC, 1992, pp. 594–602.

[19]Tyc, G., "OEDIPUS-A Attitude Determination Study Using Magnetometer Data," Bristol Aerospace Ltd., ER 91906/A, Winnipeg, MB, Canada, Dec. 1991.

[20]Boutin, B. A., "OEDIPUS-A Tether Orientation Relative to the Local Magnetic Field Determined from ITT Video Camera Data," Bristol Aerospace Ltd., ER 93852/A, Winnipeg, MB, Canada, June 1993.